Title
Quantifying the Influence of Defects on Selectivity of Electrodes Encapsulated by Nanoscopic Silicon Oxide Overlayers

Journal
ACS Applied Materials & Interfaces, 14(50)

ISSN
1944-8244

Authors
Stinson, William DH
Brayton, Kelly M
Ardo, Shane
et al.

Publication Date
2022-12-21

DOI
10.1021/acsami.2c13646

ACS APPLIED MATERIALS & INTERFACES

www.acsami.org

Research Article

Quantifying the Influence of Defects on Selectivity of Electrodes Encapsulated by Nanoscopic Silicon Oxide Overlayers

William D. H. Stinson, Kelly M. Brayton, Shane Ardo, A. Alec Talin, and Daniel V. Esposito*

Cite This: *ACS Appl. Mater. Interfaces* 2022, 14, 55480−55490

Read Online

ACCESS | Metrics & More | Article Recommendations | Supporting Information

ABSTRACT: Encapsulation of electrocatalysts and photocatalysts with semipermeable nanoscopic oxide overlayers that exhibit selective transport properties is an attractive approach to achieve high redox selectivity. However, defects within the overlayers—such as pinholes, cracks, or particle inclusions—may facilitate local high rates of parasitic reactions by creating pathways for facile transport of undesired reactants to exposed active sites. Scanning electrochemical microscopy (SECM) is an attractive method to determine the influence of defects on macroscopic performance metrics thanks to its ability to measure the relative rates of competing electrochemical reactions with high spatial resolution over the electrode. Here, we report the use of SECM to determine the influence of overlayer defects on the selectivity of silicon oxide (SiO_x) encapsulated platinum thin-film electrocatalysts operated under conditions where two competing reactions—the hydrogen evolution and Fe(III) reduction reactions—can occur. After an SECM methodology is described to determine spatially resolved selectivity, representative selectivity maps are correlated with the location of defects that are characterized by optical, electron, and atomic force microscopies. This analysis reveals that certain types of defects in the oxide overlayer are responsible for ∼60−90% of the partial current density toward the undesired Fe(III) reduction reaction. By correcting for defect contributions to Fe(III) reduction rates, true Fe(III) permeability values for the SiO_x overlayers were determined to be over an order of magnitude lower than permeabilities determined from analyses that ignore the presence of defects. Finally, different types of defects were studied revealing that defect morphology can have varying influence on both redox selectivity and calculated permeability. This work highlights the need for spatially resolved measurements to evaluate the performance of oxide-encapsulated catalysts and understand their performance limits.

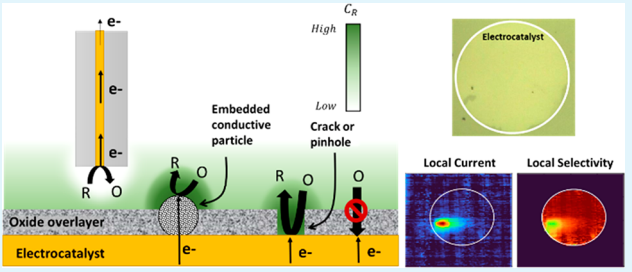

KEYWORDS: *scanning electrochemical microscopy, electrocatalysis, photocatalysis, correlative microscopy, hydrogen evolution, selectivity, oxide overlayers, defects, silicon oxide*

I. INTRODUCTION

Fuels derived from electrochemical and photoelectrochemical devices powered by renewable energy are expected to play a key role in decarbonizing society and achieving a sustainable energy future.[1−3] For many (photo)electrochemical devices, energy efficiency is a key performance metric that has a large impact on cost competitiveness and land-use requirements.[2,4] Reaction selectivity is a typical driver of system efficiency and balance of system costs for a wide range of (photo)-electrochemical processes for which undesired, competing reactions can occur, including but not limited to CO_2 reduction, N_2 reduction, seawater electrolysis, and water splitting in the presence of redox mediators. Across all of these systems, undesired competing reactions generally reduce product yield and increase the cost of downstream separation requirements. Therefore, it is highly desirable to maximize reaction selectivity toward the desired product(s).

One method for enhancing reaction selectivity of (photo)-electrocatalytic materials is to encapsulate active site(s) with ultrathin (1−20 nm thick), semipermeable oxide overlayers possessing membrane-like transport properties. During operation, such oxide overlayers can selectively block transport of undesired reactants to the buried active sites while permitting appreciable fluxes of the desired reactants and products, thereby increasing selectivity toward the desired chemistry.[5−8] Silicon oxide (SiO_x) overlayers have proven to be especially effective for a wide variety of electrochemical reactions due to their (electro)chemical stability across a wide range of conditions and their tunable properties.[9−11] Additionally, semipermeable oxide overlayers can also be used to tune reaction kinetics at the oxide/catalyst buried interface[12] and/or to protect the underlying active (photo)electrocatalyst from degradation[13] or poisoning.[12]

Received: August 3, 2022
Accepted: November 17, 2022
Published: December 6, 2022

Many of the advanced functionalities enabled by oxide overlayers rely on a continuous coverage of the underlying active catalyst by the overlayer. However, oxide-encapsulated electrodes commonly contain defects such as pinholes, cracks, or inclusions that protrude through the overlayer,[12] which may facilitate locally high rates of unwanted reactions, decreasing the selectivity of the electrode toward the desired reaction (see Figure 1). From a metrology standpoint, nonuniform reaction

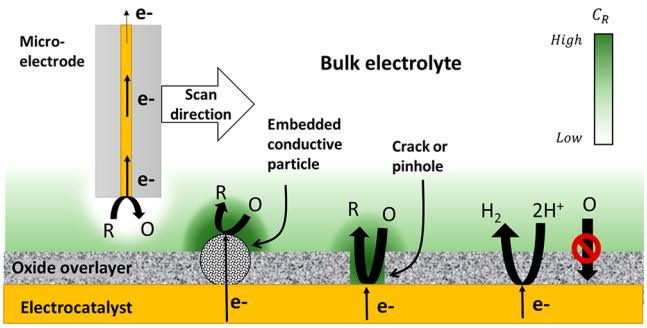

Figure 1. Schematic illustrating locally elevated product concentrations associated with high reaction rates at defects in an oxide-encapsulated electrocatalyst and the use of a scanning microelectrode to probe local reaction rates using scanning electrochemical microscopy (SECM). By independently controlling potentials of the substrate and microelectrode, SECM can be used to determine the relative amounts of both desired and undesired reaction products evolved as a function of spatial position and compared with the locations of defects identified using complementary techniques.

rates can lead to overestimates of reactant permeabilities. Similar parallels can be drawn to ultrathin oxides used for carrier selective junctions in photovoltaic cells, where pinholes can significantly alter the cell performance.[14,15] It is therefore highly desirable to determine the influence of defects on the performance of oxide encapsulated (photo)electrocatalysts.

Scanning electrochemical microscopy (SECM) is well-suited for measuring the influence of nano- or microscopic defects on electrochemical selectivity[16−18] thanks to its ability to nondestructively measure local electrochemical properties of electrode surfaces using a scanning nano- or microscopic electrode.[19−21] Of particular relevance to the current study, SECM has previously been used to understand the influence of defects in protective corrosion inhibition layers[22−25] and shown differences in activity toward different redox species.[26,27] As illustrated in Figure 1 for commonly employed substrate-generation-tip collection (SG/TC) experiments, redox species generated at the substrate can be subsequently converted at the tip of the microelectrode, resulting in an electrochemical current that is measured independently from the substrate current using a bipotentiostat. As the SECM tip is typically positioned within 2−3 probe radii of the substrate, the signal measured by the microelectrode primarily arises from conversion of electroactive species generated beneath the tip and therefore is proportional to the local reaction rate on the substrate underneath the tip. By scanning the probe over a given area of the substrate, SECM can be used to generate spatially resolved activity maps of heterogeneous electrodes to reveal the local dependence of electrochemical reaction rates on materials composition, structure, and/or morphology.[28−32] At this probe−substrate separation distance, there is minimal positive/negative feedback with the substrate, which can complicate quantitative analysis. Typically, SECM is used to study systems with only one reaction occurring at a time but has occasionally been used in systems containing multiple competing redox reactions or pathways.[26,27,33−37] In such cases, attempts to measure spatial differences in selectivity during operation are rare. When multiple redox reactions occur on an electrode that are characterized by sufficiently different standard reduction potentials, the applied potential can be altered to detect one or both species, allowing for determination of partial currents associated with each reaction and thereby selectivity, at microscopic locations on the surface.

Here, we use SECM to determine the influence of defects on the selectivity and calculated transport properties of species through silicon oxide overlayers deposited on Pt thin films. As a basis for this study, the hydrogen evolution reaction (HER) in acid (eq 1) and the ferric ion reduction reaction (FeRR, eq 2) were chosen as the two competing reactions of interest.

$$2H^+ + 2e^- \rightarrow H_2 \qquad E^0_{H^+/H_2} = 0.00\ \text{V vs NHE} \tag{1}$$

$$Fe(III) + e^- \rightarrow Fe(II) \qquad E^0_{Fe(III)/Fe(II)} = 0.77\ \text{V vs NHE} \tag{2}$$

Within the aqueous sulfate solutions used for this study, the ferric and ferrous ions exist as both aquo- and sulfate complexes,[38] but will be referred to as Fe(III) and Fe(II) for simplicity throughout this article. Both the HER and FeRR are known to have fast kinetics on Pt in acidic electrolyte.[39] However, the FeRR has a substantially more positive standard reduction potential (E^0) compared to the onset potential of the HER, resulting in a ≈ 0.77 V potential window where FeRR can be selectively detected. Furthermore, due to different hydrated radii and chemical interactions with silicon oxide, Fe(III) is expected to be selectively blocked by SiO_x compared to H^+[40]. By using these competing reactions, we demonstrate that local partial currents can be determined through independent control of the applied potentials of the substrate and the SECM tip. Features appearing in images of SECM-derived activity can then be correlated with the physical and chemical properties of defects measured by other microscopies to establish what types of defects are detrimental to reaction selectivity. These SECM images can then be used to determine (i) the contribution of defects to the overall rate of the undesired reaction and (ii) true species permeabilities within the overlayer after correcting for the contributions of defects. This analysis shows that failure to account for defects can result in effective permeability values that drastically overestimate the value of the true permeability of a defect-free overlayer.

II. METHODS AND MATERIALS

2.1. Electrode Fabrication. Electrodes were prepared from monocrystalline, degenerately doped silicon wafer (prime grade, p^+-Si(100), resistivity <0.005 Ω-cm, 500−550 μm thick, University Wafer). A 3 nm thick platinum (Pt) layer and 2 nm of Ti adhesion layer were electron-beam deposited onto the silicon wafer under a high vacuum (<6 × 10^{-8} Torr) at a rate of 0.5 Å s^{-1} for planar electrodes. A shadow mask (Photo Sciences Inc.) was used to define a 500 μm diameter disk for SECM electrodes. Silicon oxide overlayers were deposited using a low-temperature photochemical synthesis method described elsewhere.[41] The entire deposition process was completed twice, targeting 5 nm of SiO_x for each deposition, to create a bilayer 10 nm SiO_x structure. Electrical connections were made to the back of the silicon wafer using conductive copper tape and silver conductive paint (Pt disk samples) or copper wire attached through indium solder (planar electrodes). Planar electrodes were sealed with

https://doi.org/10.1021/acsami.2c13646
ACS Appl. Mater. Interfaces 2022, 14, 55480−55490

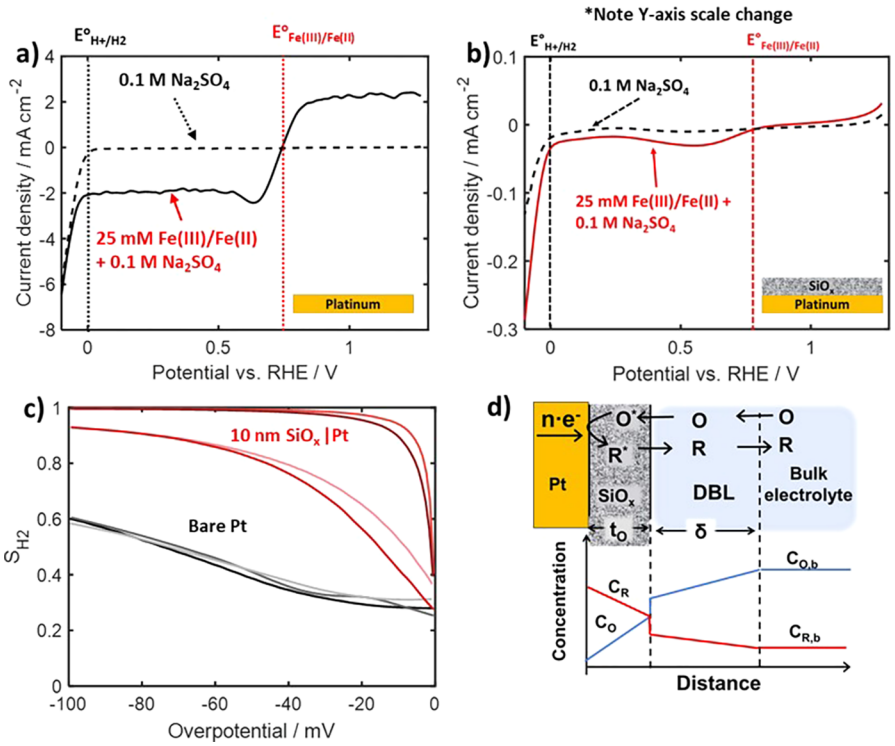

Figure 2. Cyclic voltammograms (negative potential scan only) at 20 mV s^{-1} in Fe-free supporting electrolyte (100 mM Na_2SO_4 + 50 mM H_2SO_4, pH 1.5) and Fe-containing electrolyte (12.5 mM $Fe_2(SO_4)_3$ + 25 mM $FeSO_4$ + 100 mM Na_2SO_4 + 50 mM H_2SO_4, pH 1.5) with representative (a) bare platinum electrode and (b) 10 nm SiO_x encapsulated Pt electrode. Note that the *y*-axis is scaled differently for (a) and (b). (c) Selectivity toward the HER for both electrodes plotted as a function of overpotential, with black and gray traces corresponding to three different bare Pt samples, and the red traces corresponding to four different 10 nm SiO_x|Pt samples, with details seen in Figure S2. (d) Side-view illustration of representative concentration profiles for a reduced (R) and oxidized (O) species during steady state reaction at the buried interface of a planar SiO_x|Pt electrode in the absence of migration or defects. The distance (x) in (d) is not drawn to scale. DBL = diffusion boundary layer.

electroplating tape (3M). Current densities for all samples were calculated by normalizing the substrate current by the geometric area of Pt exposed to the electrolyte.

2.2. Materials Characterization. Silicon oxide overlayer thicknesses were measured using a J.A. Wollam Alpha-SE ellipsometer. For Pt disk samples, measurements were completed on the bare silicon area and estimated to be of similar thickness over the Pt disk. X-ray photoelectron spectroscopy (XPS) imaging was carried out using a Thermo Fisher Scientific ESCALAB QXi, with details provided in the Supporting Information Section SIII. Scanning electron microscopy was conducted using a Sigma Zeiss VP scanning electron microscope, with an energy dispersive X-ray spectroscopy attachment (Bruker xFlash 6 | 30 Detector). Atomic force microscopy (AFM) was conducted using a Bruker Dimension Icon atomic force microscope in air using a ScanAsyst 25 nm radius silicon tip with a nitride lever silicon cantilever. Optical micrographs were taken using a Leica DM2700 M confocal microscope with a 5× objective lens.

2.3. Electrochemical Measurement. Electrochemical measurements were performed in deaerated iron(III) sulfate pentahydrate (≥97.0%, Thermo Scientific) and iron(II) sulfate heptahydrate (BioReagent, ≥ 99.0%, Sigma-Aldrich) in 100 mM sodium sulfate (ACS reagent grade, ≥ 99.0% anhydrous, Sigma-Aldrich) + 50 mM sulfuric acid (Certified ACS plus, Fisher Scientific) aqueous electrolyte prepared using 18 MΩ-cm deionized water. The electrolyte was adjusted to pH 1.5 using concentrated sulfuric acid and sodium hydroxide (Certified ACS, Fisher Scientific). Three-electrode electrochemical measurements reported in Section 3.1 were conducted using a Biologic SP-200 potentiostat and a commercial Ag|AgCl (aq 3 M KCl) reference electrode in 12.5 mM Fe(III) and 25 mM Fe(II) aqueous electrolyte. SECM measurements were conducted using a CH Instruments 920D bipotentiostat and carried out in a custom designed Teflon holder in 12.5 mM Fe(III) and 3 mM Fe(II) aqueous electrolyte. A commercial platinum 10 μm diameter SECM electrode (CH Instruments, CHI116) was used as the SECM probe, with optical characterization of the probe tip provided in the Supporting Information Section SXIV. A platinum wire was used as a pseudoreference electrode, where the potential stabilized near $E_{Fe(III)/Fe(II)}$ and was calibrated to RHE based on the onset potential of the HER for the SECM probe. A graphite rod (Saturn Industries, EDM3MINI12X.1100) was used as a counter electrode. The electrolyte was prepurged with nitrogen gas (Purity Plus 99.999% purity) or argon gas (Purity Plus 99.999% purity) for 1 h before the start of measurements and blanketed over the cell during measurements. The SECM tip was positioned ≈25 μm above the surface of the electrode for all experiments, determined through approach curves (Figure S16). A linear backgrounding procedure was used to correct for small transient and electrolyte compositional differences between runs as described in more detail in the Supporting Information Section SXV.

III. RESULTS AND DISCUSSION

3.1. Global Behavior of Silicon Oxide Encapsulated and Bare Electrodes. The global (i.e., macroscopic) performance of SiO_x-encapsulated Pt planar electrodes was first characterized by carrying out cyclic voltammetry (CV) in an Fe-free supporting electrolyte (100 mM Na_2SO_4 + 50 mM H_2SO_4) and those containing Fe (12.5 mM $Fe_2(SO_4)_3$ + 25 mM $FeSO_4$ + 100 mM Na_2SO_4 + 50 mM H_2SO_4) while stirring. Single scan segments recorded during the negative sweep of CV measurements (LSV) for representative bare Pt and 10 nm SiO_x|Pt thin film electrodes are provided in Figure 2a,b, respectively, with additional repeat measurements provided in Figure S2. In the Fe-free supporting electrolyte, the only notable feature for either electrode is cathodic current

https://doi.org/10.1021/acsami.2c13646
ACS Appl. Mater. Interfaces 2022, 14, 55480−55490

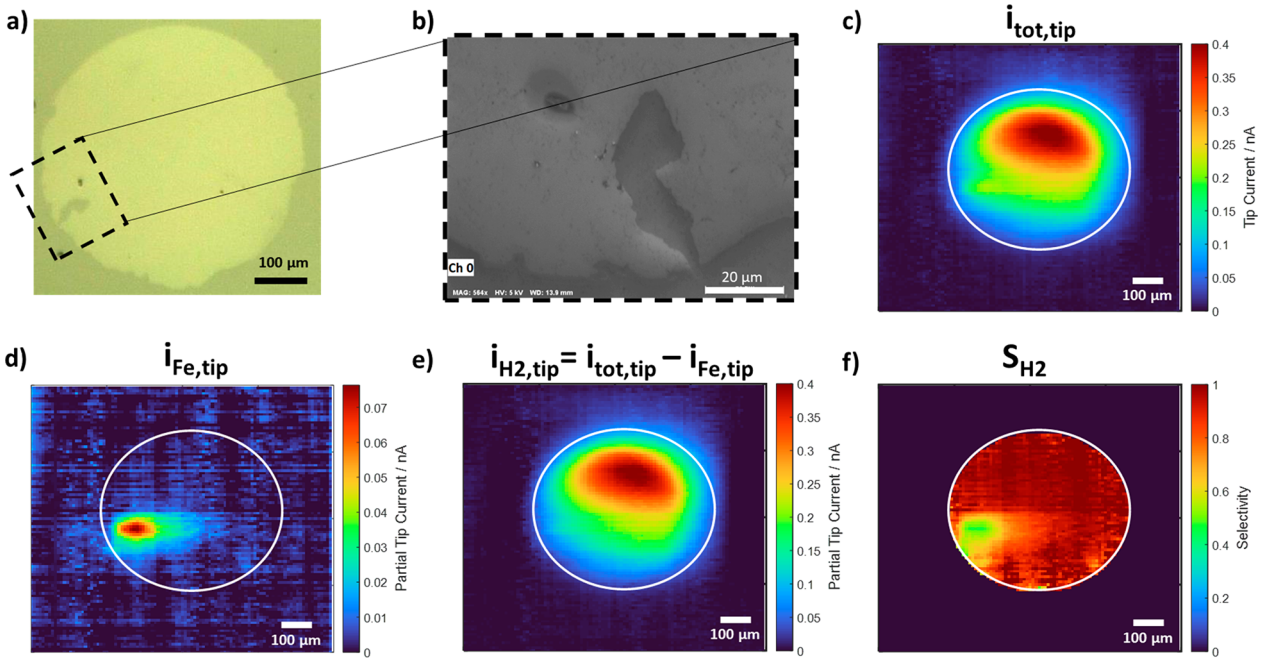

Figure 3. (a) Optical image of 10 nm SiO_x|Pt disk electrode and (b) higher resolution SEM image of area of interest. SECM images showing the tip current recorded for substrate potentials (c) of −0.050 V vs RHE, where both the HER and the FeRR occur, and (d) + 0.1 V vs RHE, where only the FeRR occurs. In (d), the partial tip current for oxidation of Fe(II) evolved from the substrate ($i_{Fe,tip}$) was calculated by subtracting background signal associated with Fe(II) oxidation from the bulk electrolyte, as described in the text. All SECM measurements were carried out in substrate generation, tip collection mode using a tip potential of 1.2 V vs RHE and an Fe-containing electrolyte (12.5 mM $Fe_2(SO_4)_3$ + 25 mM $FeSO_4$ + 100 mM Na_2SO_4 + 50 mM H_2SO_4, pH 1.5). (e) Image of the H_2 partial tip current generated based on the difference in the spatially varying total tip current ($i_{tot,tip}$) from (c) and Fe only current ($i_{Fe,tip}$) from d). (f) SECM-derived image of local selectivity toward hydrogen (S_{H_2}) over the Pt disk electrode. White lines are added for visual aids to show the Pt disk region.

associated with the HER at potentials more negative than 0.0 V vs RHE. Consistent with previous studies,[12,41] the 10 nm SiO_x overlayer results in a notable suppression of the HER signal compared to bare Pt, which is amplified due to the weakly acidic nature of the solution. When Fe(II) and Fe(III) are added to the electrolyte, the LSV curve for the bare Pt electrode displays a sharp increase in current around $E_{Fe(III)/Fe(II)}$ and mass-transfer limiting current densities for FeRR and Fe(II) oxidation (FeOR) of ≈2−3 mA cm^{-2} for overpotentials larger than 200 mV with respect to $E_{Fe(III)/Fe(II)}$. These limiting current densities are associated with diffusion of the Fe species across the diffusion boundary layer and are thus highly dependent on the rate of convective stirring of the bulk electrolyte. As seen in Figure 2b, FeRR and FeOR limiting current densities are also observed for the 10 nm SiO_x|Pt electrode but are less than 50 μA cm^{-2} across the potential range of interest. Given that SiO_x overlayers themselves display negligible activity toward Fe(II)/Fe(III) redox reactions (Figure S1), this dramatic suppression of Fe(II)/Fe(III) electrochemistry is attributed to the ability of the SiO_x overlayers to largely block dissolved Fe species from reaching Pt active sites at the buried SiO_x|Pt interface, consistent with a recent atomistic simulation study.[40]

For potentials negative of E_{H^+/H_2} where both the HER and FeRR can occur, the selectivity toward the desired H_2 product (S_{H_2}) can be quantified from the partial current densities for the HER (i_{H_2}) and the FeRR (i_{Fe}), as shown in eq 3:

$$S_{H_2} = \frac{i_{H_2}}{i_{H_2} + \frac{n_{H_2}}{n_{Fe}} i_{Fe}} \quad (3)$$

where n_{H_2} and n_{Fe} are the stoichiometric number of electrons per H_2 and Fe(II) produced in the HER and FeRR, respectively. In the analysis carried out here based on the LSV curves in Figure 2, i_{Fe} is assumed to be constant at all potentials below ≈0.6 V vs RHE and equal to the mass transfer limiting current density ($i_{lim,Fe}$). $i_{lim,Fe}$ is calculated as the average current density recorded between 0.42 and 0.52 V vs RHE to limit the influence of current arising from hydrogen underpotential adsorption occurring below 0.3 V vs RHE for polycrystalline Pt.[42] In determining $i_{lim,Fe}$, the background signal was removed by subtracting currents observed in experiments that used supporting electrolyte only. Additionally, it is assumed that the small rates of the HER occurring at low overpotentials do not affect $i_{lim,Fe}$. Since the total current density (i) measured at potentials <0.0 V vs RHE is given by the sum of i_{Fe} and i_{H_2}, i_{H_2} was determined by subtracting $i_{lim,Fe}$ from i as a function of potential and substituted into eq 3 to plot S_{H_2} between 0.0 and −0.1 V vs RHE in Figure 2c. Comparing the S_{H_2} vs potential curves for SiO_x|Pt to bare Pt, it is seen that all 10 nm SiO_x samples display significant increases in selectivity toward H_2. At −0.05 V vs RHE, S_{H_2} > 80% is seen for all SiO_x|Pt compared to only ≈40% for bare Pt. However, large variation in selectivity can be seen for the four SiO_x|Pt electrodes analyzed in Figure 2c although all were fabricated using nominally the same procedure. The sample-to-sample variation in selectivity arises largely from the variation in the determined $i_{lim,Fe}$ signal, which varies from 2 to 100 μA cm^{-2}. Such variations may arise from differences in defect populations across samples, although slight differences in experimental conditions cannot be ruled out.

https://doi.org/10.1021/acsami.2c13646
ACS Appl. Mater. Interfaces 2022, 14, 55480−55490

Another important characteristic of a semipermeable overlayer is its permeability toward reactant species j (P_j).[43,44] By assuming a solution-diffusion model with one-dimensional (1D) transport across a diffusion boundary layer and through a uniform overlayer (Figure 2d, eq 4), P_j can be estimated from an experimentally measured steady-state $i_{lim,j}$ value using eq 5:[43,44]

$$i_{lim,j} = \frac{n_j F C_{j,b}}{\frac{1}{k_c} + \frac{t_o}{P_j}} \quad (4)$$

$$P_j = t_o \cdot \left(\frac{n_j F C_{j,b}}{i_{lim,j}} - \frac{1}{k_c} \right)^{-1} \quad (5)$$

where n_j is the stoichiometric number of electrons per species j, F is the Faraday constant, $C_{j,b}$ is the bulk concentration of species j, t_o is the overlayer thickness, and k_c is the mass transfer coefficient associated with the diffusion boundary layer. For overlayers characterized by $(P_j/t_o) \ll (k_c)$, most of the concentration change in the limiting reactant occurs across the overlayer rather than the diffusion boundary layer, and $(1/k_c)$ in eq 5 can be ignored.

Using the FeRR limiting current densities from the global LSV measurements as inputs to eq 4, the permeability of Fe(III) through the SiO_x overlayer was calculated to range from 1.8×10^{-13} to 1.0×10^{-11} cm^2 s^{-1} for four different 10 nm SiO_x|Pt electrodes, with a mean value of $3.0 \pm 4.9 \times 10^{-12}$ cm^2 s^{-1}. Similar to the analysis of selectivity in Figure 2c, the relatively large range of calculated $P_{Fe(III)}$ values is a direct consequence of the large variation in the measured $i_{lim,Fe}$ values. Nonetheless, all values of $P_{Fe(III)}$ were orders of magnitude less than H^+ permeabilities (P_{H^+}) previously reported for similarly prepared SiO_x overlayers (1.7×10^{-11}[12] to 1×10^{-7} cm^2 s^{-1}[9]), indicating that such coatings strongly favor H^+ transport over Fe(III). The large difference in $P_{Fe(III)}$ and P_{H^+} could be attributed to differences in diffusion mechanisms for the two different permeants. The inability of Fe(III) to participate in hydrogen-bonding or chemically interact with SiO_x suggests that it likely diffuses through pores or other breaks in the overlayer, unlike H^+ which diffuses via a Grotthuss mechanism involving "proton hopping" along the hydrogen bond network of the oxide, as suggested by computational studies.[45,46] Previous characterization by ellipsometric porosimetry of SiO_x overlayers made by the same method employed here indicated that pores, if they exist, are <5.8 Å.[12] Given that the hydrated radii for Fe(III) is 4.6 Å and for H^+ is 2.8 Å,[47] it is therefore no surprise that $P_{Fe(III)} << P_{H^+}$, which also explains the significantly enhanced selectivity toward the HER over the FeRR for SiO_x-encapsulated electrodes.

3.2. Spatially-Resolved Selectivity Measurements. In the previous section, the reported effective permeabilities were calculated assuming that the SiO_x overlayer is defect-free and homogeneous with respect to structure (e.g., thickness, porosity) and composition. To locally measure the relative rates of the HER and the FeRR, we utilized SECM with a well-defined 500 μm diameter Pt disk electrode (Figure 3a) serving as a fiducial marker that facilitated correlative microscopy measurements with SECM, scanning electron microscopy (SEM), energy-dispersive X-ray spectroscopy (EDS), optical microscopy, and atomic force microscopy (AFM).

Three separate SECM images were generated using SG/TC mode. For all three images, the applied potential at the tip was held constant at 1.2 V vs RHE, which allows for oxidation of both H_2 and Fe(II) product species generated at the substrate. The applied potential at the substrate was varied between one of three different values to control which product species were generated at the substrate during SECM measurements: (i) open-circuit potential (OCP), which results in little-to-no production of either H_2 or Fe(II), (ii) +0.1 V vs RHE, which results in the mass-transfer-limited FeRR, and (iii) −0.05 V vs RHE, which results in both the HER and the FeRR. A substrate potential of −0.05 V vs RHE was chosen to keep the generation of H_2 below rates that would lead to bubble formation, which would create undesirable noise. Electrolytes used for SECM measurements contained 25 mM Fe(III) and 3 mM Fe(II), where the lowered concentration of Fe(II) was chosen to decrease the background signal at the tip associated with Fe(II) oxidation from the bulk electrolyte and also stabilize the pseudoreference electrode.

An SECM image recorded using a substrate potential of −0.05 V vs RHE and showing the total tip signal ($i_{tot,tip}$) associated with both the HER and the FeRR in the vicinity of the SiO_x-encapsulated Pt disk is shown in Figure 3c. Negligible signal was detected for probe positions located further than 100 μm away from the physical edge of the Pt disk, which is marked with the white outline in all images. This observation indicates that the surface of the p^+-Si(100) substrate is inert toward both the HER and the FeRR at this substrate potential. Partial tip current associated with Fe(II) species evolved from the substrate ($i_{Fe,tip}$) was calculated from the difference in tip currents measured during scans completed with substrate applied potentials of 0.1 V vs RHE and OCP, which removes the background signal associated with the FeOR from Fe(II) species initially present in the bulk solution. The resulting SECM image of $i_{Fe,tip}$, shown in Figure 3d, reveals elevated signal originating from the bottom left region of the disk. This localized signal is also seen in Figure 3c at the same location but is less apparent due to the much larger tip response associated with oxidation of H_2 generated by the disk at the more negative substrate potential. Tip current associated with H_2 oxidation ($i_{H_2,tip}$) was then calculated from the difference in tip currents measured for substrate potentials of −0.05 and +0.1 V vs RHE, with the resulting image of i_{H_2} shown in Figure 3e. The localized signal seen in the left corner of Figure 3c is no longer visible in the i_{H_2} image, suggesting that the rate of HER is relatively uniform in this region. Some differences in the H_2 signal over the entire disk electrode are observed, which could result from nonuniform overlayer thickness. XPS spatial maps of a similarly prepared sample did not indicate any significant variation in thickness over the disk sample (Figure S3). This was confirmed through an additional sample for which SECM imaging was carried out in Fe-free and Fe-containing electrolytes during electrode operation at +0.1 and −0.05 V vs RHE (Figure S19). The resulting SECM images of HER current were both uniform and of similar magnitude in both electrolytes, providing confidence that the subtraction process used to generate partial HER signal in the Fe-containing electrolyte is accurate.

Once SECM images of tip signal associated with two competing reactions are obtained, they can be used to calculate local selectivity of the substrate toward H_2 on a pixel-by-pixel basis using eq 6:

https://doi.org/10.1021/acsami.2c13646
ACS Appl. Mater. Interfaces 2022, 14, 55480−55490

$$S_{H_2} = \frac{i_{H_2,tip}}{i_{H_2,tip} + \left(\frac{n_{H_2}}{n_{Fe}}\right)\left(\frac{CE_{H_2}}{CE_{Fe}}\right) i_{Fe,tip}} \quad (6)$$

where CE_j is the collection efficiency of the SECM probe toward product species j, which represents the fraction of species j produced at the substrate electrode that is subsequently collected at the probe. CE is largely dependent on geometric variables (tip radius, tip/substrate distance, etc.), which is constant for each scan. Since the tip is also operating at a large overpotential for both reactions, it is reasonable to assume that both product species should be collected to the same degree, and therefore the collection efficiency term can be dropped from eq 6. This was experimentally confirmed by carrying out microelectrode CV scans while positioning the probe tip over the center of a platinum feature under a range of partial HER and FeRR current densities (Figure S4). Local S_{H_2} values were then calculated using eq 6 and plotted as a function of probe position throughout the scan as shown in Figure 3f. These images demonstrate that selectivity is not uniform but rather locally depressed in the region of the sample that exhibits locally higher Fe(III) reduction current in Figure 3d.

To better understand the origin of the locally high FeRR current, correlative microscopy was carried out using SEM (Figure 3b) and EDS analysis (Figure S5) of the same Pt disk analyzed by SECM. An SEM image of the area responsible for the high FeRR current (Figure 3b) displays both a break in the platinum disk and a ≈5 μm diameter particulate defect. EDS compositional images of this region (Figure S6) reveal that the particle defect has higher carbon and oxygen content than the surrounding areas while maintaining similar platinum signal, suggesting that the particle defect is organic in nature and not a platinum particle protruding through the SiO_x overlayer. No additional large breaks in the oxide overlayer, either around the defect or over the edge of the platinum (Figure S7), could be observed in AFM images, though the entire area was not scanned. However, breaks in the oxide are not likely as the HER current is relatively uniform over the highlighted region in Figure 3b. If the underlying platinum layer was exposed or the overlayer thinned, a higher local HER current would be expected in addition to the higher local FeRR current. Alternatively, carbon particles have been demonstrated to catalyze simple, outer sphere electrochemical reactions while exhibiting poor HER kinetics.[48] Therefore, it is plausible that the carbonaceous particle is the cause for the local FeRR current. This hypothesis was validated through additional experimentation using glassy carbon particles as surrogate defects (Figure S15).

From the SECM-derived selectivity image in Figure 3f, it is apparent that the defect or cluster of defects in the lower left portion of the disk electrode has a substantial impact on S_{H_2}. While S_{H_2} is seen to be consistently >97% across most of the disk electrode, S_{H_2} drops to ≈50% in the vicinity of this defect. As a result, the average S_{H_2} value for the sample is 93%, determined using the sum of partial currents per pixel over the disk from the SECM images in Figure 3c,d, similar to the values for macroscopic electrodes in a N_2-purged round-bottom flask setup seen in Figure 2c. However, this average S_{H_2} derived from SECM measurements carried out for a substrate potential of −0.05 V vs RHE is substantially greater than the value of 57% for this same disk sample using the analysis of LSV curves described in Section 3.1. The lower selectivity value obtained from LSV using eq 3 is most likely due to additional current from side reactions, such as the oxygen reduction reaction, whose products are poorly detected using SECM. This was validated by additional experiments using heavier argon gas to blanket the SECM cell, which reduces the flux of oxygen (Supporting Information Section SXVI).

3.3. Determination of True Species Permeabilities. To obtain a more accurate measure of $P_{Fe(III)}$, it is necessary to remove the influence of localized FeRR current occurring at defects for which Fe(III) species are not actually diffusing through the overlayer. This can be done by recognizing that the FeRR current ($i_{lim,Fe}$) passing through the entire electrode equals the sum of currents due to Fe(III) transport through defects (i_d) and through the overlayer (i_o). Assuming that the collection efficiency for the Fe(II) product at the SECM tip is the same regardless of whether Fe(II) is formed at a defect or a buried interface, SECM measurements can be used to quantify the fraction of FeRR current occurring through the overlayer ($i_{o,tip}/i_{Fe,tip}$) for the entire electrode. Under these conditions, the ratio determined from SECM measurements will be equal to the ratio occurring at the substrate. i_o is then a simple product of this ratio and the total substrate current, which when inserted into eq 5 for $i_{lim,Fe}$, yields the true permeability of Fe(III) through the overlayer without the influence of defects.

For the following analysis, $i_{o,tip}$, was calculated by averaging the background-subtracted FeRR current over all pixels coinciding with the disk location except those clearly affected by the defect in the lower left-hand portion of the disk, as visualized in Figure S8. This average value of $i_{o,tip}$ was then subtracted from each value of $i_{Fe,tip}$ at every pixel, with the difference being attributed to additional FeRR current originating from the defect ($i_{d,tip}$). Summing values for $i_{d,tip}$ and values for $i_{o,tip}$ over the disk area revealed that i_d was 6.7 times larger than i_o, meaning that ≈87% of the total tip current associated with FeRR while scanning over the Pt disk electrode originated from the defect(s) located in the lower left portion of the disk. The ratio of overlayer to total current ($i_{o,tip}/i_{Fe,tip}$) was then multiplied by $i_{lim,Fe}$, taken from LSV data obtained from the substrate, to calculate i_o, and plugged back into eq 5 for $i_{lim,Fe}$, to estimate $P_{Fe(III)}$ to be $2.3 \pm 0.3 \times 10^{-12}$ cm^2 s^{-1} without the influence of defects. This defect-compensated "true" permeability (P_{true}) is nearly an order of magnitude lower from the uncompensated estimate of $1.4 \pm 0.2 \times 10^{-11}$ cm^2 s^{-1}, which was calculated using the same procedure as in Section 3.1 (Table S1). This analysis demonstrates that even a single defect can result in significantly overestimated values of P_j if the current occurring at defects is not taken into account.

To more generally explore the discrepancies between P_{eff} and P_{true} arising from defects, a pseudo-1D model was created for a generic species j. A hypothetical scenario was used, where an encapsulated electrode contains multiple identical hemispherical defect particles with radius (a) of 5 μm that protrude through a 10 nm thick overlayer. Within this model, which is describe in more detail in the Supporting Information Section SIX, eq 7 was used to calculate the current that arises from reaction at unencapsulated defect sites that were assumed to be spaced far enough apart that they operate independently from each other.

$$i_d = 2\pi n_j F C_{j,b} D_j a \quad (7)$$

https://doi.org/10.1021/acsami.2c13646
ACS Appl. Mater. Interfaces 2022, 14, 55480−55490

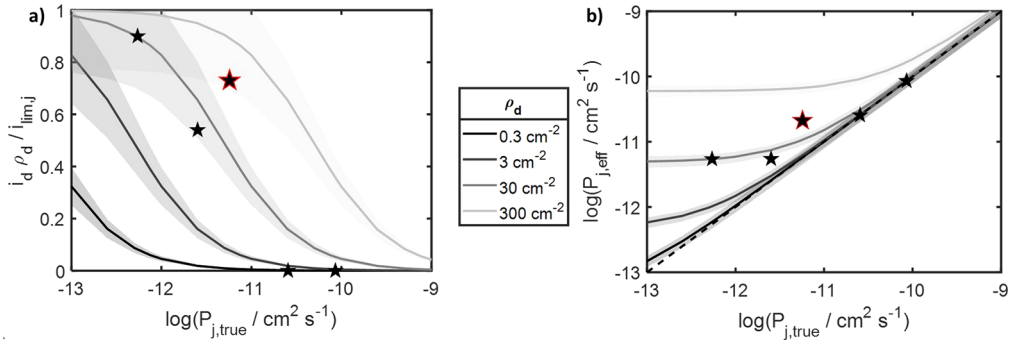

Figure 4. Modeling the effects of overlayer defect density (ρ_d) in a planar oxide encapsulated electrode on (a) the percentage of the total electrode current passing through defects as a function of the true permeability of the reactant species within the overlayer and (b) the effective species permeability as a function of true permeability. For both panels, the shaded areas indicate relative error in $i_d\rho_d/i_{lim,j}$ calculated by propagating 1% error on all input parameters (r, t_o, δ, D). It is assumed that the reaction of interest is operating under mass-transfer-limited conditions. Defects consist of hemispherical particles with radius (a) = 5 μm and are assumed to operate independent of each other according to eq 7. Current generated by species diffusion through the overlayer (i_o) was modeled using eq 4, with t_o = 10 nm. In (b), the dashed line indicates agreement between the effective (calculated) and true permeabilities, which is the case when there are zero defects. Data from SECM samples, shown in Table S3 are included (black stars), where the defect current was estimated from SECM partial current maps. SECM corrected permeability for Fe(III) was plotted as $P_{j,true}$, and $P_{j,eff}$ is the uncompensated $P_{Fe(III)}$. The sample from Section 3.2 is outlined in red.

eq 4 was used to calculate the limiting current density arising from diffusion of species j through the overlayer (i_o), for a range of assumed $P_{j,true}$. Finally, the total current density of the electrode, $i_{lim,j}$, was computed using eq 8,

$$i_{lim,j} = \rho_d i_d + i_o(1 - A_d\rho_d) \quad (8)$$

where ρ_d is the defect density (*i.e.* defects) and A_d is the 2-dimensional area surrounding each defect where $C_j \ll C_{j,b}$ such that negligible reaction occurs at the buried interface in that area. In Figure 4a, the fraction of current passing through the defects ($i_d\rho_d/i_{lim,j}$) is plotted as a function of $P_{j,true}$ for four different defect densities. The parameters for both eqs 4 and 7 were adopted from the sample seen in Section 3.2, where t_o = 10 nm and $k_c = 2.4 \times 10^{-4}$ cm s^{-1}. As expected, the defects contribute a higher fraction of the total current for high defect densities and low $P_{j,true}$. By substituting $i_{lim,j}$ into eq 5, the effective permeability ($P_{j,eff}$) can then be computed and compared to $P_{j,true}$, which can be seen in Figure 4b. $P_{j,eff}$ is seen to be significantly larger than $P_{j,true}$ whenever defect density is high and $P_{j,true}$ is very small. Conversely, good agreement between $P_{j,true}$ and $P_{j,eff}$ is achieved for lower defect densities and a higher $P_{j,true}$. For these conditions, permeabilities may reliably be calculated using the method outlined in Section 3.1. Data from SECM experiments (black stars) are added to Figure 4, where $i_d/i_{lim,j}$ was calculated from SECM partial current images, $P_{j,true}$ is the SECM corrected $P_{Fe(III)}$, and $P_{j,eff}$ is the uncompensated $P_{Fe(III)}$. Consistent with expectation, the data point in Figure 4a corresponding to the sample from Section 3.2 (black star with red outline) is located close to the modeled curve for ρ_d = 30 defects cm^{-2}, which corresponds to 1 defect per 500 μm diameter disk as observed experimentally. This provides additional evidence that the single carbon defect is likely accounting for >60% of the total current, leading to approximately an order of magnitude overestimate of uncompensated $P_{Fe(III)}$ relative to the true $P_{Fe(II)}$. The other black stars appearing in Figure 4 correspond to other 10 nm SiO$_x$|Pt disk electrode samples analyzed by SECM and also follow the trend predicted by the model, with those samples exhibiting the lowest Fe(III) permeabilities giving the biggest discrepancy between the effective and true permeability values. These additional samples help validate the model and suggest that defect-mediated current is a large proportion of their total current, which results in $P_{j,eff} > P_{j,true}$ for these low P_j overlayers.

3.4. Identification of Different Types of Overlayer Defects. To better understand how specific defect types influence SiO$_x$|Pt electrode selectivity, additional samples were fabricated and their spatially resolved activity evaluated using the same SECM methodology outlined in Section 3.2 and seen in the Supporting Information Section SXVI. Through these investigations, it was discovered that multiple types of defects are common on SiO$_x$|Pt samples and that they can exhibit very different behavior toward the HER and the FeRR. Figure 5a shows an optical microscope image of one SiO$_x$|Pt electrode for which three defects characterized by different morphologies are located in close proximity, allowing for their impact on selectivity to be simultaneously assessed using SECM. One of these defects (defect #1, Figure 5d) is a particulate defect that is located ≈100 μm beyond the edge of the platinum disk and is easily observable thanks to its large diameter of ≈8 μm, while defects at location #2 and #3 are barely visible by optical microscopy. However, defects #2 and #3 are observed to have a disproportionately large influence on the electrochemical selectivity of the electrode, as seen in the SECM-determined partial current images for the HER and the FeRR in Figure 5b,c, respectively. SECM does not detect any H_2 or Fe(II) signal originating from defect #1, while defects #2 and #3 both coincide with the observation of locally elevated current associated with the FeRR. Figure 5b also shows that defect #2 results in locally elevated HER current that is greater than that measured anywhere else on the sample.

To better elucidate the origins of the different HER and FeRR behavior of these three defects, each area was further characterized by SEM, EDS, and/or AFM. EDS reveals that defect #1 is primarily comprised of titanium and oxygen (Figure S12), suggesting that this defect is a particle generated during electron-beam evaporation of the Ti adhesion layer. This particle likely underwent oxidation during the overlayer curing process, resulting in the formation of titanium oxide (TiO$_x$) on its surface. SEM imaging does not display the presence of any particle protrusions around defect #2 (Figure 5e) but does display the presence of cracks seen near the edge of the platinum feature. AFM analysis of one crack, located

https://doi.org/10.1021/acsami.2c13646
ACS Appl. Mater. Interfaces 2022, 14, 55480−55490

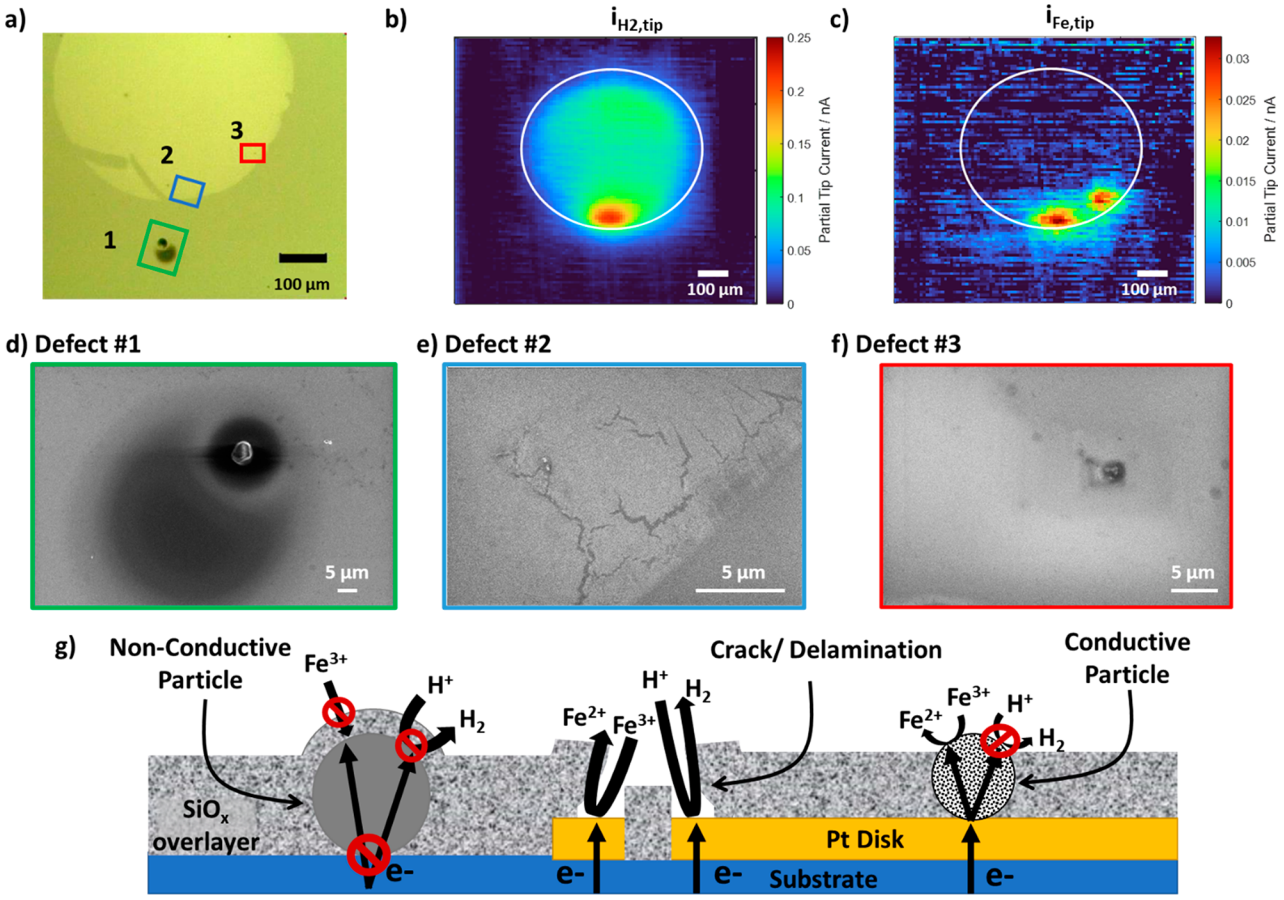

Figure 5. (a) Optical image with colored rectangles indicating the location of three distinct defects on a 10 nm thick SiO_x|500 μm diameter Pt disk electrode supported on an inert p^+-Si(100) substrate. Partial tip current associated with (b) the HER and (c) the FeRR. White lines are added as visual aids for location of the edges of the Pt disk electrode. Higher resolution SEM images of (d) defect #1 displaying a Ti/TiO_x particle, (e) defect #2 displaying cracks in the SiO_x overlayer, and (f) defect #3 displaying a carbonaceous particle. (g) Generalized schematic illustrating the electrochemical behavior of all three types of defects identified on this sample.

near the top of Figure 5e and oriented perpendicular to the edge of the disk, is characterized by elevated features that run parallel to the crack (Figure S13). This morphology suggests that the SiO_x overlayer peeled upward on either side of the crack, which may result in exposure of the underlying Pt catalyst to the bulk electrolyte. This description is consistent with the observation of locally elevated $i_{Fe,tip}$ and $i_{H_2,tip}$ in the vicinity of location 2, since direct exposure of Pt to H^+ and Fe(III) in the electrolyte is expected to lead to increases in both the HER and the FeRR. SEM (Figure 5f), EDS, and AFM (Figure S14) confirmed that defect #3 was an exposed carbon particle, similar to that identified in Figure 3b, which also exhibited an increase in FeRR current and no additional HER activity.

In comparing the physical and chemical characteristics of the two particle defects, the main difference largely lies in the chemical composition. While Ti/TiO_x is largely a poor HER catalyst, it can be relatively active toward simple redox reactions. However, the particle may also be inactive due to (i) lack of an electronically conductive pathway between the substrate and outer surface of the particle or (ii) encapsulation by the SiO_x overlayer, which is at least expected to block the FeRR as already shown for the SiO_x-covered Pt disk. The behavior of the three different defects observed in Figure 5b,c is summarized in Figure 5g, which highlights how different types of defects can have substantially differing effects on redox selectivity.

IV. CONCLUSIONS

This study showed that defects represent an important consideration in the development of oxide overlayers for selective (photo)electrocatalysts and that SECM can be a valuable tool for analyzing their effects on key performance metrics like selectivity and species permeabilities. Our analysis across 11 different 500 μm diameter Pt disk electrodes showed that only one or two isolated defects are often responsible for 60−90% of currents for the FeRR, having a disproportionate influence on decreasing the selectivity of the SiO_x|Pt electrode toward the HER.

In addition to showing that a small number of overlayer defects can have a large impact on an electrode's selectivity, this study demonstrated that failure to account for defect-contributed current can greatly overestimate species permeability values that are calculated from steady-state one-dimensional diffusion models based on experimentally measured mass-transfer-limited current densities for the entire electrode. To account for this discrepancy, a methodology was developed that uses SECM measurements to determine the fraction of signal arising from defects and uses that quantity to determine a corrected or "true" species permeability for which defect-contributed signal has been excluded. When applied to

https://doi.org/10.1021/acsami.2c13646
ACS Appl. Mater. Interfaces 2022, 14, 55480−55490

model SiO_x|Pt disk electrodes, this analysis method revealed that the permeability of Fe(III) through 10 nm SiO_x overlayers can easily be overestimated by an order of magnitude if defects are not accounted. Using a modified one-dimensional diffusion model that accounts for varying densities of noninteracting hemispherical defects, this study also established the relationship between true and effective (i.e., measured) species permeabilities, highlighting the fact that the biggest discrepancies in species permeabilities arise from cases where the true permeabilities are low and defect densities are high.

Lastly, this study showed that individual defects can exhibit vastly different behavior toward the competing HER and FeRR and consequently have varying influence on the selectivity. By employing correlative microscopy in which complementary imaging methods are used to analyze the chemical and physical properties of the same defects, structure−property relationships of different defect types were uncovered. Some defects were observed to increase the local current due to both the HER and the FeRR, only the FeRR, or neither reaction. Overall, this study highlights the importance of quantifying the influence of defects on the selectivity of oxide-encapsulated (photo)electrocatalysts and presents methodologies that may be applied to a wide range of materials and chemistries beyond those investigated in this work.

■ ASSOCIATED CONTENT

Supporting Information

The Supporting Information is available free of charge at https://pubs.acs.org/doi/10.1021/acsami.2c13646.

Figures of CV curves, SEM image, collection efficiencies, SEM and EDS of samples, AFM imaging, SECM FeRR partial current image, 1D diffusional profile, simulated electrode current and defect current using a 1D transport model plotted versus permeability, SECM approach curve, example of linear background subtraction procedure completed on three line scans, example of linear background subtraction procedure, current images and mapping, permeability modeling curves, and optical and SECM partial current maps, discussions of XPS imaging, quantitative determination of selectivity, calculating SECM-derived compensated permeabilities, 1D diffusional model with defects of known size, surrogate particle defects using glassy carbon particles, and background subtraction procedure, and tables of mass transfer-limited FeRR current densities and tip current ratios and estimated permeabilities (PDF)

■ AUTHOR INFORMATION

Corresponding Author

Daniel V. Esposito − *Department of Chemical Engineering, Columbia Electrochemical Engineering Center, Lenfest Center for Sustainable Energy, Columbia University in the City of New York, New York, New York 10027, United States;* orcid.org/0000-0002-0550-801X; Email: de2300@columbia.edu

Authors

William D. H. Stinson − *Department of Chemical Engineering, Columbia Electrochemical Engineering Center, Lenfest Center for Sustainable Energy, Columbia University in the City of New York, New York, New York 10027, United States*

Kelly M. Brayton − *Department of Chemical Engineering, Columbia Electrochemical Engineering Center, Lenfest Center for Sustainable Energy, Columbia University in the City of New York, New York, New York 10027, United States*

Shane Ardo − *Department of Chemistry, Department of Chemical and Biomolecular Engineering, and Department of Materials Science and Engineering, University of California Irvine, Irvine, California 92697, United States;* orcid.org/0000-0001-7162-6826

A. Alec Talin − *Materials Physics Department, Sandia National Laboratories, Livermore, California 94550, United States;* orcid.org/0000-0002-1102-680X

Complete contact information is available at: https://pubs.acs.org/10.1021/acsami.2c13646

Author Contributions

The manuscript was written through contributions of all authors. All authors have given approval to the final version of the manuscript.

Notes

The authors declare no competing financial interest.

■ ACKNOWLEDGMENTS

The authors acknowledge funding from the Department of Energy, Office of Energy Efficiency and Renewable Energy and specifically the HydroGEN Advanced Water Splitting Materials Consortium, established as part of the Energy Materials Network under this same office (Award No. DE-EE0008838). The authors also thank Dr. Tim Nunney at Thermo Fisher Scientific for carrying out XPS imaging experiments. The authors acknowledge the use of facilities and instrumentation supported by NSF through the Columbia University, Columbia Nano Initiative, and the Materials Research Science and Engineering Center DMR-2011738. Sandia National Laboratories is a multimission laboratory managed and operated by National Technology and Engineering Solutions of Sandia, LLC., a wholly owned subsidiary of Honeywell International, Inc., for the U.S. Department of Energy's National Nuclear Security Administration under contract DE-NA-0003525. This paper describes objective technical results and analyses. Any subjective views or opinions that might be expressed in the paper do not necessarily represent the views of the U.S. Department of Energy or the United States Government.

■ ABBREVIATIONS USED

i_j	partial current density toward reaction j
$i_{lim,j}$	mass-transfer limiting current density toward reaction j
n_j	stoichiometric number of electrons per species j
S_j	selectivity toward desired product j
P_j	permeability toward reactant species j
$C_{b,j}$	bulk solution concentration of reactant species j
D_j	diffusion coefficient of species j
k_c	mass transfer coefficient associated with the diffusion boundary layer
t_o	silicon oxide overlayer thickness
F	Faraday constant
$i_{j,tip}$	partial current occurring on SECM tip from reactant j
CE_j	SECM tip collection efficiency associated with species j

i_o current density occurring from reaction at SiOx| electrode interface
i_d current occurring from reaction at hemispherical defect
$P_{j,eff}$ effective permeability of reactant species j
$P_{j,true}$ true permeability of reactant species j
ρ_d defect density
a defect radius
A_d diffusional area of defect
δ_o diffusion boundary layer thickness of electrode
δ_d diffusion boundary layer thickness of hemispherical particle defect

REFERENCES

(1) Ardo, S.; Fernandez Rivas, D.; Modestino, M. A.; Schulze Greiving, V.; Abdi, F. F.; Alarcon Llado, E.; Artero, V.; Ayers, K.; Battaglia, C.; Becker, J.-P.; Bederak, D.; Berger, A.; Buda, F.; Chinello, E.; Dam, B.; Di Palma, V.; Edvinsson, T.; Fujii, K.; Gardeniers, H.; Geerlings, H. H.; Hashemi, S. M.; Haussener, S.; Houle, F.; Huskens, J.; James, B. D.; Konrad, K.; Kudo, A.; Kunturu, P. P.; Lohse, D.; Mei, B.; Miller, E. L.; Moore, G. F.; Muller, J.; Orchard, K. L.; Rosser, T. E.; Saadi, F. H.; Schüttauf, J.-W.; Seger, B.; Sheehan, S. W.; Smith, W. A.; Spurgeon, J.; Tang, M. H.; Van De Krol, R.; Vesborg, P. C. K.; Westerik, P. Pathways to electrochemical solar-hydrogen technologies. *Energy Environ. Sci.* **2018**, *11* (10), 2768−2783.

(2) Kim, J. H.; Hansora, D.; Sharma, P.; Jang, J.-W.; Lee, J. S. Toward practical solar hydrogen production - an artificial photosynthetic leaf-to-farm challenge. *Chem. Soc. Rev.* **2019**, *48* (7), 1908−1971.

(3) Chen, C.; Khosrowabadi Kotyk, J. F.; Sheehan, S. W. Progress toward commercial application of electrochemical carbon dioxide reduction. *Chem.* **2018**, *4* (11), 2571−2586.

(4) Pinaud, B. A.; Benck, J. D.; Seitz, L. C.; Forman, A. J.; Chen, Z.; Deutsch, T. G.; James, B. D.; Baum, K. N.; Baum, G. N.; Ardo, S.; Wang, H.; Miller, E.; Jaramillo, T. F. Technical and economic feasibility of centralized facilities for solar hydrogen production via photocatalysis and photoelectrochemistry. *Energy Environ. Sci.* **2013**, *6* (7), 1983−2002.

(5) Vos, J. G.; Wezendonk, T. A.; Jeremiasse, A. W.; Koper, M. T. M. MnOx/IrOx as selective oxygen evolution electrocatalyst in acidic chloride solution. *J. Am. Chem. Soc.* **2018**, *140* (32), 10270−10281.

(6) Maeda, K.; Teramura, K.; Lu, D. L.; Saito, N.; Inoue, Y.; Domen, K. Noble-metal/Cr_2O_3 core/shell nanoparticles as a cocatalyst for photocatalytic overall water splitting. *Angew. Chem. Int. Edit* **2006**, *45* (46), 7806−7809.

(7) Garcia-Esparza, A. T.; Shinagawa, T.; Ould-Chikh, S.; Qureshi, M.; Peng, X.; Wei, N.; Anjum, D. H.; Clo, A.; Weng, T.-C.; Nordlund, D.; Sokaras, D.; Kubota, J.; Domen, K.; Takanabe, K. An oxygen-insensitive hydrogen evolution catalyst coated by a molybdenum-based layer for overall water splitting. *Angew. Chem., Int. Ed.* **2017**, *56* (21), 5780−5784.

(8) Chen, S. S.; Vequizo, J. J. M.; Pan, Z. H.; Hisatomi, T.; Nakabayashi, M.; Lin, L. H.; Wang, Z.; Kato, K.; Yamakata, A.; Shibata, N.; Takata, T.; Yamada, T.; Domen, K. Surface modifications of $(ZnSe)_{0.5}(CuGa_{2.5}Se_{4.25})_{0.5}$ to promote photocatalytic z-scheme overall water splitting. *J. Am. Chem. Soc.* **2021**, *143* (28), 10633−10641.

(9) Beatty, M. E. S.; Gillette, E. I.; Haley, A. T.; Esposito, D. V. Controlling the relative fluxes of protons and oxygen to electrocatalytic buried interfaces with tunable silicon oxide overlayers. *ACS Appl. Energy Mater.* **2020**, *3* (12), 12338−12350.

(10) Takenaka, S.; Miyazaki, T.; Matsune, H.; Kishida, M. Highly active and durable silica-coated Pt cathode catalysts for polymer electrolyte fuel cells: Control of micropore structures in silica layers. *Catal. Sci. Technol.* **2015**, *5* (2), 1133−1142.

(11) Jo, W. J.; Katsoukis, G.; Frei, H. Ultrathin amorphous silica membrane enhances proton transfer across solid-to-solid interfaces of stacked metal oxide nanolayers while blocking oxygen. *Adv. Funct. Mater.* **2020**, *30* (12), 1909262.

(12) Labrador, N. Y.; Songcuan, E. L.; De Silva, C.; Chen, H.; Kurdziel, S. J.; Ramachandran, R. K.; Detavernier, C.; Esposito, D. V. Hydrogen evolution at the buried interface between Pt thin films and silicon oxide nanomembranes. *ACS Catal.* **2018**, *8* (3), 1767−1778.

(13) Labrador, N. Y.; Li, X.; Liu, Y.; Tan, H.; Wang, R.; Koberstein, J. T.; Moffat, T. P.; Esposito, D. V. Enhanced performance of Si MIS photocathodes containing oxide-coated nanoparticle electrocatalysts. *Nano Lett.* **2016**, *16* (10), 6452−6459.

(14) Peibst, R.; Römer, U.; Larionova, Y.; Rienäcker, M.; Merkle, A.; Folchert, N.; Reiter, S.; Turcu, M.; Min, B.; Krügener, J.; Tetzlaff, D.; Bugiel, E.; Wietler, T.; Brendel, R. Working principle of carrier selective poly-Si/c-Si junctions: Is tunnelling the whole story? *Sol. Energy Mater. Sol. Cells* **2016**, *158*, 60−67.

(15) Yang, Z.; Liu, Z.; Cui, M.; Sheng, J.; Chen, L.; Lu, L.; Guo, W.; Yang, X.; Zhao, Y.; Yang, W.; Greer, J. C.; Zeng, Y.; Yan, B.; Ye, J. Charge-carrier dynamics for silicon oxide tunneling junctions mediated by local pinholes. *Cell Rep. Phys. Sci.* **2021**, *2* (12), 100667.

(16) Pust, S. E.; Maier, W.; Wittstock, G. Investigation of localized catalytic and electrocatalytic processes and corrosion reactions with scanning electrochemical microscopy (SECM). *Z. Phys. Chem.* **2008**, *222* (10), 1463−1517.

(17) Niu, L.; Yin, Y.; Guo, W.; Lu, M.; Qin, R.; Chen, S. Application of scanning electrochemical microscope in the study of corrosion of metals. *J. Mater. Sci.* **2009**, *44* (17), 4511−4521.

(18) Pishgar, S.; Gulati, S.; Strain, J. M.; Liang, Y.; Mulvehill, M. C.; Spurgeon, J. M. In situ analytical techniques for the investigation of material stability and interface dynamics in electrocatalytic and photoelectrochemical applications. *Small Methods* **2021**, *5* (7), 2100322.

(19) Polcari, D.; Dauphin-Ducharme, P.; Mauzeroll, J. Scanning electrochemical microscopy: A comprehensive review of experimental parameters from 1989 to 2015. *Chem. Rev.* **2016**, *116* (22), 13234−13278.

(20) Fernández, J. L.; Walsh, D. A.; Bard, A. J. Thermodynamic guidelines for the design of bimetallic catalysts for oxygen electroreduction and rapid screening by scanning electrochemical microscopy. M-co (M: Pd, Ag, Au). *J. Am. Chem. Soc.* **2005**, *127* (1), 357−365.

(21) Simpson, B. H.; Rodríguez-López, J. Electrochemical imaging and redox interrogation of surface defects on operating $SrTiO_3$ photoelectrodes. *J. Am. Chem. Soc.* **2015**, *137* (47), 14865−14868.

(22) González-García, Y.; Santana, J. J.; González-Guzmán, J.; Izquierdo, J.; González, S.; Souto, R. M. Scanning electrochemical microscopy for the investigation of localized degradation processes in coated metals. *Prog. Org. Coat.* **2010**, *69* (2), 110−117.

(23) Upadhyay, V.; Battocchi, D. Localized electrochemical characterization of organic coatings: A brief review. *Prog. Org. Coat.* **2016**, *99*, 365−377.

(24) Basame, S. B.; White, H. S. Scanning electrochemical microscopy: Measurement of the current density at microscopic redox-active sites on titanium. *J. Phys. Chem.B* **1998**, *102* (49), 9812−9819.

(25) Casillas, N.; Charlebois, S. J.; Smyrl, W. H.; White, H. S. Scanning electrochemical microscopy of precursor sites for pitting corrosion on titanium. *J. Electrochem. Soc.* **1993**, *140* (9), L142−L145.

(26) Basame, S. B.; White, H. S. Chemically-selective and spatially-localized redox activity at Ta/Ta_2O_5 electrodes. *Langmuir* **1999**, *15* (3), 819−825.

(27) Basame, S. B.; White, H. S. Scanning electrochemical microscopy of native titanium oxide films. Mapping the potential dependence of spatially-localized electrochemical reactions. *J. Phys. Chem.* **1995**, *99* (44), 16430−16435.

(28) Limani, N.; Boudet, A.; Blanchard, N.; Jousselme, B.; Cornut, R. Local probe investigation of electrocatalytic activity. *Chem. Sci.* **2021**, *12* (1), 71−98.

(29) Preet, A.; Lin, T.-E. A review: Scanning electrochemical microscopy (SECM) for visualizing the real-time local catalytic activity. *Catalysts* **2021**, *11* (5), 594.

https://doi.org/10.1021/acsami.2c13646
ACS Appl. Mater. Interfaces 2022, 14, 55480−55490

(30) Chen, X.; Botz, A. J. R.; Masa, J.; Schuhmann, W. Characterisation of bifunctional electrocatalysts for oxygen reduction and evolution by means of SECM. *J. Solid State Electrochem* **2016**, *20* (4), 1019−1027.
(31) Hanekamp, P.; Raith, T.; Iffelsberger, C.; Zankl, T.; Robl, W.; Matysik, F.-M. Material contrast studies of conductive thin films on semiconductor substrates using scanning electrochemical microscopy. *J. Appl. Electrochem.* **2019**, *49* (5), 455−463.
(32) Aaronson, B. D. B.; Chen, C. H.; Li, H. J.; Koper, M. T. M.; Lai, S. C. S.; Unwin, P. R. Pseudo-single-crystal electrochemistry on polycrystalline electrodes: Visualizing activity at grains and grain boundaries on platinum for the Fe2+/Fe3+ redox reaction. *J. Am. Chem. Soc.* **2013**, *135* (10), 3873−3880.
(33) Mayer, F. D.; Hosseini-Benhangi, P.; Sánchez-Sánchez, C. M.; Asselin, E.; Gyenge, E. L. Scanning electrochemical microscopy screening of CO_2 electroreduction activities and product selectivities of catalyst arrays. *Commun. Chem.* **2020**, *3* (1), 1−9.
(34) Leonard, K. C.; Bard, A. J. The study of multireactional electrochemical interfaces via a tip generation/substrate collection mode of scanning electrochemical microscopy: The hydrogen evolution reaction for Mn in acidic solution. *J. Am. Chem. Soc.* **2013**, *135* (42), 15890−15896.
(35) Lee, W.; Lee, T.; Kim, S.; Bae, S.; Yoon, J.; Cho, K. Descriptive role of Pt/ptox ratio on the selective chlorine evolution reaction under polarity reversal as studied by scanning electrochemical microscopy. *ACS Appl. Mater. Interfaces* **2021**, *13* (29), 34093−34101.
(36) Rodríguez-López, J.; Alpuche-Avilés, M. A.; Bard, A. J. Interrogation of surfaces for the quantification of adsorbed species on electrodes: Oxygen on gold and platinum in neutral media. *J. Am. Chem. Soc.* **2008**, *130* (50), 16985−16995.
(37) Zigah, D.; Rodríguez-López, J.; Bard, A. J. Quantification of photoelectrogenerated hydroxyl radical on TiO_2 by surface interrogation scanning electrochemical microscopy. *Phys. Chem. Chem. Phys.* **2012**, *14* (37), 12764.
(38) Casas, J. M.; Crisóstomo, G.; Cifuentes, L. Speciation of the Fe(ii)-Fe(iii)-H_2SO_4-H_2O system at 25 and 50°c. *Hydrometallurgy* **2005**, *80* (4), 254−264.
(39) Hansen, J. N.; Prats, H.; Toudahl, K. K.; Mørch Secher, N.; Chan, K.; Kibsgaard, J.; Chorkendorff, I. Is there anything better than Pt for HER? *ACS Energy Lett.* **2021**, *6* (4), 1175−1180.
(40) Aydin, F. S.; Sharma, S.; Zagalskaya, A.; Maiti, A.; Esposito; Daniel, V.; Ardo, S.; Pham, T. A.; Ogitsu, T.Transport of Redox Shuttles in Microporous Silicon Oxide Films: Mechanistic Insights from Molecular Dynamics Simulations, in press.
(41) Beatty, M. E. S.; Chen, H.; Labrador, N. Y.; Lee, B. J.; Esposito, D. V. Structure-property relationships describing the buried interface between silicon oxide overlayers and electrocatalytic platinum thin films. *J. Mater. Chem. A* **2018**, *6* (44), 22287−22300.
(42) Łosiewicz, B.; Jurczakowski, R.; Lasia, A. Kinetics of hydrogen underpotential deposition at polycrystalline platinum in acidic solutions. *Electrochim. Acta* **2012**, *80*, 292−301.
(43) Esposito, D. V.; Guilimondi, V.; Vos, J. G.; Koper, M. T. M., Chapter 7. Design principles for oxide-encapsulated electrocatalysts. In *Energy and environment series*; Frei, H., Esposito, D., Eds.; Royal Society of Chemistry: Cambridge, 2022; pp 167−209.
(44) Esposito, D. V. Membrane-coated electrocatalysts—an alternative approach to achieving stable and tunable electrocatalysis. *ACS Catal.* **2018**, *8* (1), 457−465.
(45) Godet, J.; Pasquarello, A. Proton diffusion mechanism in amorphous SiO_2. *Phys. Rev. Lett.* **2006**, *97* (15), 155901.
(46) Kurtz, H. A.; Karna, S. P. Proton mobility in a-SiO_2. *IEEE Trans. Nucl. Sci.* **1999**, *46* (6), 1574−1577.
(47) Nightingale, E. R. Phenomenological theory of ion solvation. Effective radii of hydrated ions. *J. Phys. Chem.* **1959**, *63* (9), 1381−1387.
(48) McCreery, R. L. Advanced carbon electrode materials for molecular electrochemistry. *Chem. Rev.* **2008**, *108* (7), 2646−2687.

https://doi.org/10.1021/acsami.2c13646
ACS Appl. Mater. Interfaces 2022, 14, 55480−55490